and Chemistry of the Actinides, A. J. Freeman, G. H. Lander, Eds. (North-Holland, Amsterdam, 1987), vol. 5, pp. 311–372.

22. We thank the staff of beamline ID30 and the safety group at the ESRF for their help and the U.S. Department of Energy (DOE) for the use of transplutonium elements, which were produced in the High Flux Isotope Reactor and Radiochemical Engineering Development Center at ORNL. Supported in part by the Division of Chemical Sciences, Geoscience,

On-Wire Lithography

Lidong Qin, Sungho Park, Ling Huang, Chad A. Mirkin*

We report a high-throughput procedure for lithographically processing one-dimensional nanowires. This procedure, termed on-wire lithography, combines advances in template-directed synthesis of nanowires with electrochemical deposition and wet-chemical etching and allows routine fabrication of face-to-face disk arrays and gap structures in the range of five to several hundred nanometers. We studied the transport properties of 13-nanometer gaps with and without nanoscopic amounts of conducting polymers deposited within by dip-pen nanolithography.

Despite their many attributes and capabilities, nanolithographic techniques such as electron-beam lithography, dip-pen nanolithography (DPN), focused ion-beam lithography, and nanoimprint lithography are limited with respect to throughput, materials compatibility, resolution, and cost (*1*). For example, the field of nanoelectronics depends on the ability to fabricate and functionalize electrode gaps less than 20 nm wide for precise electrical measurements on nanomaterials. Fabricating such structures is far from routine and often involves low-yielding, imprecise, and difficult-to-control procedures such as break-junction techniques and gap narrowing by electroplating (*2–6*). Here, we present a relatively high-throughput procedure for lithographically processing nanowires that allows us to control gap size down to the 5-nm length scale. This procedure, termed on-wire lithography (OWL), combines advances in template-directed synthesis of nanowires with electrochemical deposition and wet-chemical etching and allows the routine fabrication of architectures that would be difficult, if not impossible, to make with any known lithographic methodology (Scheme 1).

OWL is based on the idea that one can make segmented nanowires consisting of at least two types of materials, one that is susceptible and one that is resistant to wet-chemical etching. For proof of concept, we used Au-Ag and Au-Ni. We first describe the process involving Au-Ni nanowires. These materials can be electrochemically deposited in porous alumina templates (pore diameter = 360 nm) in a controlled fashion from suitable

plating solutions through well-established methods (Scheme 1) (*7–11*). The length of each segment can be tailored by controlling the charge passed during the electrodeposition process (fig. S1). They are released from the template by dissolution of the template through literature procedures (*12*).

The nanowire aqueous suspension was cast on a glass microscope slide, pretreated with piranha solution to make it hydrophilic, and allowed to dry in a dessicator. A layer of silica (50 nm) was deposited on the nanowire-coated substrate by plasma-enhanced chemical vapor deposition (*13*). The substrate was immersed in ethanol and sonicated (VWR Ultrasonic Cleaner, MODEL 50T) for 1 min, which resulted in the release of the wires (fig. S2).
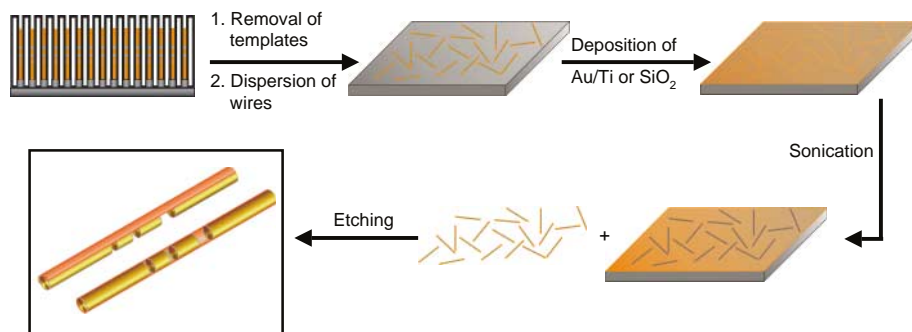
The final step of the OWL process involves the selective wet-chemical etching of the Ni segments. The Ni can be removed from the wires by treating them with concentrated HNO_3 for 1 hour to generate nanowire structures with gaps precisely controlled by the length of the original Ni segments (Scheme 1).

We also prepared similar structures using Ag as the sacrificial segment material and an Au/Ti bilayer (40 nm/10 nm) deposited by

thermal evaporation as the segment-bridging layer instead of silica. In this case, the Ag was removed by treating the wires with an etching solution consisting of methanol, 30% ammonium hydroxide, and 30% hydrogen peroxide (4:1:1 v/v/v) for 1 hour.

Using the OWL procedure, we prepared nanowires with designed gaps of 5, 25, 40, 50, 70, 100, 140, and 210 nm (Fig. 1). The physical dimensions and block compositions of the nanowires, before and after etching, were determined by field-emission scanning electron microscopy (FESEM) and energy-dispersive x-ray spectroscopy (fig. S3), respectively. Structures made of Au and Ag before coating with Au/Ti and wet-chemical etching exhibit a bright contrast for the Au regions and a dark contrast for the Ag regions (Fig. 1A). Etching then creates the notched structures (Fig. 1B). The average length of the wires (±SD) is 4.5 ± 0.25 μm, and each wire exhibits two notches measuring 210 ± 10 nm, two measuring 140 ± 8 nm, and two measuring 70 ± 5 nm (Fig. 1B). The diameter of each wire is 360 ± 20 nm. Certain views show the Au/Ti backing, which bridges the notched regions on these structures (Fig. 1B, inset). Structures with gap sizes of less than 100 nm can be routinely generated with OWL. To demonstrate this capability, we used OWL to prepare wires with 25-, 50-, and 100-nm gaps (Fig. 1C).

We observed similar results with the use of Ni as the sacrificial segment and silica as the bridging material. To demonstrate that OWL can make repeating structures consisting of regular 40-nm gaps, we made nanowire structures with 22 40-nm Ni segments and 23 40-nm Au segments (Fig. 1D). After coating with silica and subsequent removal of the Ni blocks, face-to-face disk arrays with 40-nm gaps were generated (Fig. 1E). The statistical

Department of Chemistry and Institute for Nanotechnology, Northwestern University, 2145 Sheridan Road, Evanston, IL 60208–3113, USA.

*To whom correspondence should be addressed. E-mail: chadnano@northwestern.edu

Scheme 1. OWL methodology.

variation of gap size generally increases with decreasing gap size but is typically less than 10%. The greater variation in some images is caused by mechanical stress on the wire structures, which results in a "fanning" effect with respect to the gaps. The smallest gap structures generated to date with the OWL approach are 5 nm (Fig. 1F), but with the appropriate electrochemical control, there is no reason this number cannot be reduced.

An important issue involving the characterization and utility of gaps fabricated by OWL pertains to their transport properties. In principle, for the structures prepared with the silica bridging material, one can use the micrometer-scale gold ends as electrode leads that can be interfaced with larger microelectrode electronic circuitry. Indeed, all of the structures with gaps have been characterized by current versus voltage (I-V) measurements and exhibit insulating behavior (green line in Fig. 2A). To test the

properties of these structures and their suitability for making transport measurements on small amounts of materials contained within the gaps, we evaporated a droplet of a suspension that contained wires with 13-nm gaps on a microelectrode array fabricated by conventional photolithography (Fig. 2, B and C). The electrodes were 3 μm wide and separated by 2 μm. Some of the wires ended up bridging the microelectrodes, allowing us to easily make electrical measurements on such structures.

Measurements of I-V curves show that the gaps within the nanowires are insulating (green line in Fig. 2A). The gaps within the nanowires can be functionalized with many materials in a site-specific manner using DPN (fig. S4) (14, 15). As proof of concept, we deposited a mixture of polyethylene oxide and self-doped polypyrrole (PEO:PPy = 1:1 w/w) into the gap by DPN. This approach allows us to monitor the device architecture in the active region,

measure the topography of the nanowires, and simultaneously functionalize the nanowire gaps with molecule-based materials. An SEM image after modification of the gap with polymer shows the clear contrast between the clean gold surface and the polymer-covered area including the gap (Fig. 2C, inset). After deposition of the polymer, the I-V curves show a linear response from –1.0 to 1.0 V, characteristic of the conducting polymer (red line in Fig. 2A). The measured conductance of 1.1 nS is similar to the value of 9.6 nS determined by functionalizing 60-nm conventional nanoelectrode gaps fabricated by electron-beam lithography in our lab. There is no noticeable I-V hysterisis between the forward (from –1.0 to +1.0 V) and backward (from +1.0 to –1.0 V) scans, and they are highly linear at room temperature, as expected for a structure with an ohmic-like contact in a symmetric device configuration.

Fig. 1. FESEM images of multisegment metallic Au-Ag nanowires (**A**) before and (**B**) after coating with a bilayer consisting of 10 nm of Ti and 40 nm of Au and subsequent wet-chemical etching of the Ag segments. Insets show magnified images. (**C**) Side view of a nanogap wire with gap sizes of 25, 50, and 100 nm. Multisegment metallic Au-Ni nanowires (**D**) before and (**E**) after coating one side with 50 nm of silica and subsequent wet-chemical etching of the Ni segments. Each Au and Ni segment length is 40 nm. Insets are magnified images. (**F**) An Au nanowire with a 5-nm gap. Every nanowire in the batch has a well-defined gap.
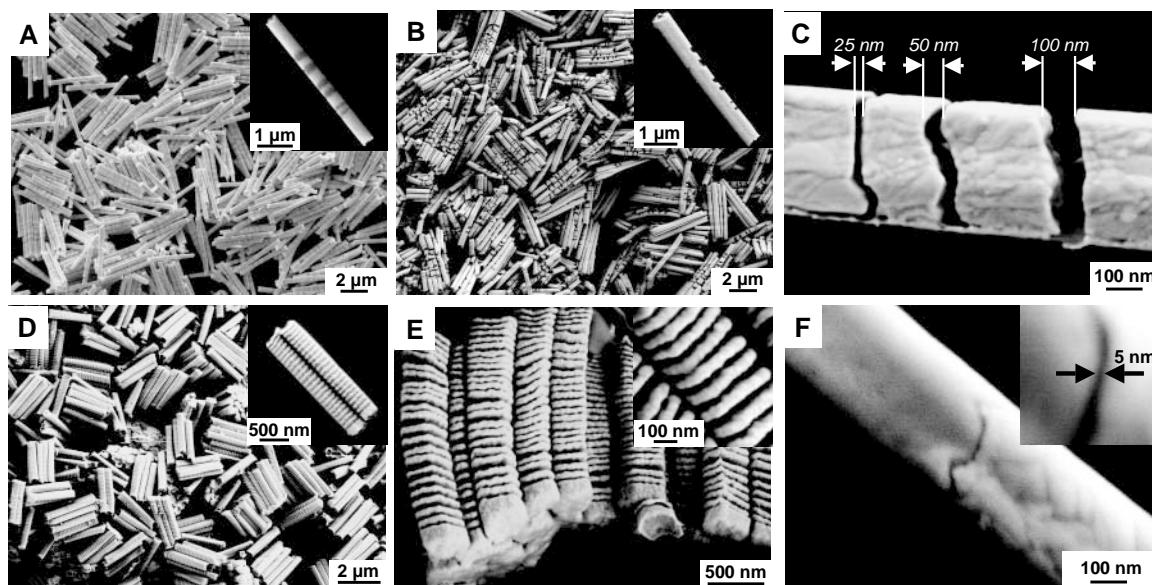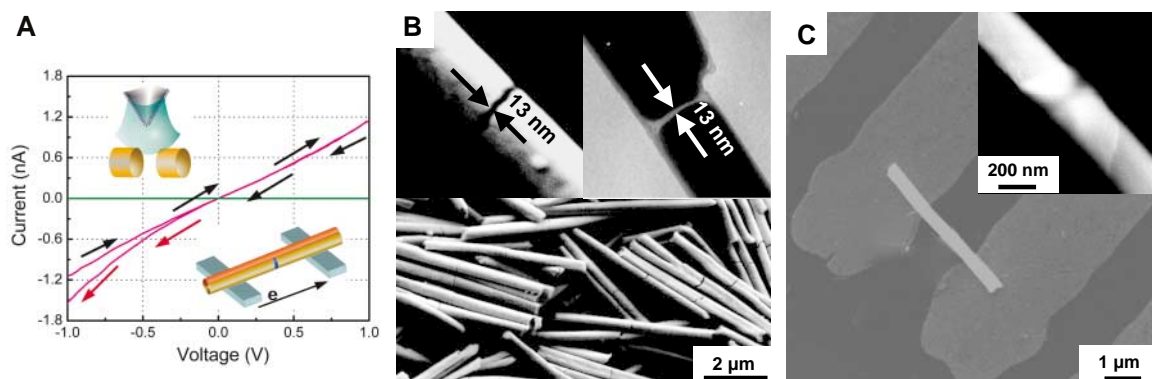

Fig. 2. (**A**) Current-voltage measurements on the wires with nanogaps. The green line is before functionalization of the gap with PPy/PEO by DPN, and the red line is after it has been filled with the polymer mixture. The inset describes the DPN process. The red arrows indicate the observed conductivity change under Xe light irradiation. e, electrons. (**B**) Images of Au wires with 13-nm gaps. In the center of each wire, the dark lines are the nanogaps. The contrast depends on which side is facing out because of the silica coating. The left inset is a magnified FESEM image of a 13-nm gap, and the right inset is a magnified transmission electron microscopy image, which shows the transparent gap. (**C**) An FESEM image of a wire with a 13-nm gap, which is immobilized on microelectrodes and filled with PPy/PEO. (Inset) An image that shows clear contrast between the clean gold surface and the polymer-covered area, including the gap. The contrast is a result of differences in substrate charging due to the presence of organic polymer.

To show that the response is indeed from the polymer within the gap, we studied the I-V response as a function of photoexcitation with a Xe lamp (150 W). The I-V response for the polymer-filled nanowire becomes slightly more conductive upon Xe light exposure. During the backward scan, the device was irradiated with the Xe lamp starting at –0.1 V (red arrows in Fig. 2A), and a change in slope in the I-V response was observed. The transient conductance change between 1.1 nS in the dark to 1.6 nS when irradiated is consistent with an increase in charge-carrier density, which would be expected if the gap were filled with the p-type polypyrrole (16).

We report a novel lithographic process that allows one to generate designed gap structures on nanowire templates. The process is remarkably controllable, high-yielding, and easy to implement. It does not require sophisticated and expensive instrumentation and facilities, and it allows manipulation of an important class of structures that cannot be easily manipulated with conventional lithographic tools. Being able to make gap or notched structures with nanowires with OWL and relatively inexpensive instrumentation will facilitate the study of the electronic properties of nanomaterials and open avenues to the preparation of novel disk structures, which could be designed to have unusual optical properties as a function of gap and metal segment size [e.g., plasmon waveguides (17)].

References and Notes
1. B. D. Gates *et al.*, *Chem. Rev.* **105**, 1171 (2005).
2. M. A. Reed, C. Zhou, C. J. Muller, T. P. Burgin, J. M. Tour, *Science* **278**, 252 (1997).
3. J. Reichert *et al.*, *Phys. Rev. Lett.* **88**, 176804 (2002).
4. H. Park, A. K. L. Lim, A. P. Alivisatos, J. Park, P. L. McEuen, *Appl. Phys. Lett.* **75**, 301 (1999).
5. C. Z. Li, H. X. He, N. J. Tao, *Appl. Phys. Lett.* **77**, 3995 (2000).
6. J. Xiang *et al.*, *Angew. Chem. Int. Ed. Engl.* **44**, 1265 (2005).
7. C. R. Martin, *Science* **266**, 1961 (1994).
8. D. Routkevitch, T. Bigioni, M. Moskovits, J. M. Xu, *J. Phys. Chem.* **100**, 14037 (1996).
9. S. R. Nicewarner-Pena *et al.*, *Science* **294**, 137 (2001).
10. N. I. Kovtyukhova, T. E. Mallouk, *Chem. Eur. J.* **8**, 4354 (2002).
11. A. K. Salem, M. Chen, J. Hayden, K. W. Leong, P. C. Searson, *Nano Lett.* **4**, 1163 (2004).
12. S. Park, J.-H. Lim, S.-W. Chung, C. A. Mirkin, *Science* **303**, 348 (2004).
13. Materials and methods are available as supporting material on *Science* Online.
14. R. D. Piner, J. Zhu, F. Xu, S. Hong, C. A. Mirkin, *Science* **283**, 661 (1999).
15. D. S. Ginger, H. Zhang, C. A. Mirkin, *Angew. Chem. Int. Ed. Engl.* **43**, 30 (2004).
16. S. Park, S.-W. Chung, C. A. Mirkin, *J. Am. Chem. Soc.* **126**, 11772 (2004).
17. S. A. Maier *et al.*, *Nat. Mater.* **2**, 229 (2003).
18. C.A.M. acknowledges the U.S. Air Force Office of Scientific Research (AFOSR), Defense Advanced Research Projects Agency (DARPA), and NSF for support of this research.

Supporting Online Material
www.sciencemag.org/cgi/content/full/309/5731/113/DC1
Materials and Methods
Figs. S1 to S4

Atlantic Ocean Forcing of North American and European Summer Climate

Rowan T. Sutton* and Daniel L. R. Hodson

Recent extreme events such as the devastating 2003 European summer heat wave raise important questions about the possible causes of any underlying trends, or low-frequency variations, in regional climates. Here, we present new evidence that basin-scale changes in the Atlantic Ocean, probably related to the thermohaline circulation, have been an important driver of multidecadal variations in the summertime climate of both North America and western Europe. Our findings advance understanding of past climate changes and also have implications for decadal climate predictions.

Instrumental records show that during the 19th and 20th centuries, there were marked variations on multidecadal time scales in the summertime climate of both North America (1–4) and western Europe (5). In the continental United States, there were significant variations in rainfall and drought frequency (1–4), and it has been suggested (1, 4) that changes in the Atlantic Ocean, associated with a pattern of variation known as the Atlantic Multidecadal Oscillation (AMO) (6, 7), were responsible. If confirmed, such a link would be important for climate predictions because the AMO is thought to be driven by the ocean's thermo-

haline circulation (6) and may be predictable (8, 9). However, thus far the evidence for an Atlantic link is mainly circumstantial, being derived from observations and showing correlation rather than causality. Clarifying whether AMO-related changes in the Atlantic Ocean were indeed responsible for the observed variations in North American summer climate and whether, in addition, there were impacts on other regions is therefore an important challenge.

Figure 1 shows the time series and pattern of North Atlantic sea surface temperatures (SSTs) that characterize the AMO during the period 1871 to 2003 (10). There are AMO warm phases in the late 19th century and from 1931 to 1960; cool phases occur from 1905 to 1925 and from 1965 to 1990. The spatial pattern shows anomalies of the same sign over the whole North Atlantic, with the largest anomalies ($\sigma \sim 0.3°C$) found just east of Newfoundland.

Natural Environment Research Council Centres for Atmospheric Science, Centre for Global Atmospheric Modelling, Department of Meteorology, University of Reading, Post Office Box 243, Earley Gate, Reading RG6 6BB, UK.

*To whom correspondence should be addressed. E-mail: r.sutton@reading.ac.uk

Fig. 1. (**A**) Index of the AMO, 1871 to 2003. The index was calculated by averaging annual mean SST observations (*29*) over the region 0°N to 60°N, 75°W to 7.5°W. The resulting time series was low-pass filtered with a 37-point Henderson filter and then detrended, also removing the long-term mean. The units on the vertical axis are °C. This index explains 53% of the variance in the detrended unfiltered index and is very similar to that shown in (*1*). (**B**) The spatial pattern of SST variations associated with the AMO index shown in (A). Shown are the regression coefficients (°C per SD) obtained by regressing the detrended SST data on a normalized (unit variance) version of the index.